OPEN ACCESS

University of BRISTOL

Peer reviewed version

University of Bristol - Explore Bristol Research

General rights

Rotated Non-uniform Sub-grids in the FDTD Method with Application to a Hemispherical Antenna Array

Chris J. Railton, *Member, IEEE*

Abstract— **The use of sub-grids in the Finite Difference Time Domain (FDTD) method to facilitate the analysis of multi-scale problems is now well established. However, many of the proposed algorithms are restricted to cases where the sub-grid and the main grid share the same Cartesian coordinate system and where the ratio of the cell sizes in the two grids have a constant integer ratio. More recently, it has been shown that sub-grids, based on Cartesian grids which are rotated with respect to the main grid, can be effectively used but the cell size ratio was still kept constant. In this contribution, the method is further generalized in order to allow non-uniform sub-grids to be used. This greatly increases the range of structures which can be efficiently analyzed. The effectiveness of the method is demonstrated by application to a 31 element hemispherical array of broadband Cavity Backed Slot (CBS) antenna elements.**

Index Terms—**FDTD methods**

I. INTRODUCTION

THE Finite Difference Time Domain (FDTD) method has been widely used for many decades as a versatile and effective method of addressing electromagnetic problems[1][2]. More recently, a number of sub-gridding schemes have been proposed to address the analysis of structures which contain fine geometrical detail and which are also electrically large, for instance [3][4][5][6][7]. However, these have only been applied to situations where the meshes are uniform and in which the cell size of the sub-grid and the main grid are in a constant integer ratio. This is a severe restriction for cases such as an antenna array where each element is, itself, a complicated structure which would be best analyzed using a non-uniform mesh. Moreover, with the exception of [7], the sub-grids are constrained to share the same Cartesian axes as the main grid. For a conformal antenna array, this is another severe restriction. An example where this is an issue is the hemispherical array of slot antenna elements used in the MARIA breast cancer detection system, described in [8] and illustrated in Figure 1, which has been previously analyzed using other methods [8][9].

This array consists of 31 Cavity Backed Slot (CBS) antenna elements distributed around a hemisphere of radius 88mm and

is designed to have a usable frequency range of 3-10GHz. Details of the dimensions of the elements are given in [9].

An efficient way to characterize this array is to discretize each element using a non-uniform sub-grid which allows a smaller cell size in the vicinity of the fine features, such as the feed lines, while reducing the computational requirements by using a larger cell size in homogeneous regions. In addition, the positions of the cell boundaries relative to metal edges can be chosen for best accuracy. Each sub-grid is then placed within the main grid at the appropriate position and with the appropriate orientation in order to create the complete model. An illustration of this is given in Figure 2.

In this contribution, the method of [7] is generalized and extended to allow the use of sub-grids which are not only rotated with respect to the main grid but which can also be non-uniform and independent of the size of the cells in the main grid. In Section II the algorithm will be described and then in Section III some results will be presented. Firstly some simple cases will be examined in order to assess and demonstrate the accuracy and stability. Secondly, the method will be applied to the characterization of the realistic case of the MARIA cancer detection antenna [8] and the results will be compared to those previously obtained direct FDTD analyses.
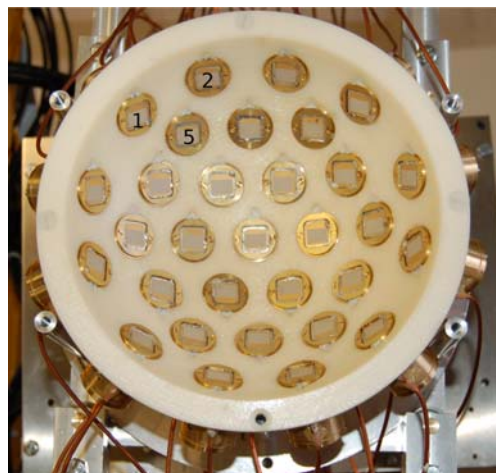

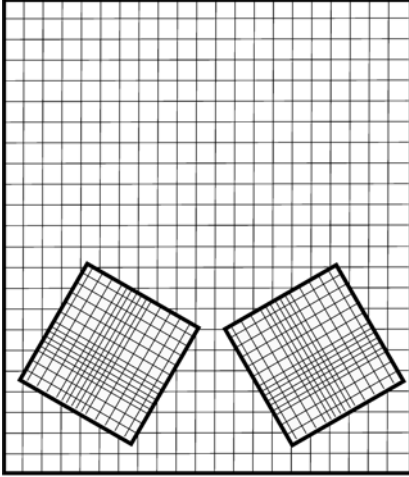**Figure 1 - The MARIA antenna array**

Figure 2 - Rotated non-uniform sub-grids used to model tilted antenna elements.

II. THE ALGORITHM

This algorithm is a direct extension of the method which is explained in detail in [7] so, in this contribution, only the modifications will be described. As in [7], the sub-grid is bounded by two surfaces, the Outer Surface, OS, and the Inner Surface, IS. This scheme is shown in Figure 3 for the case where the sub-grid is rotated with respect to the main grid by 30°. Details of the mesh around part of the Outer and Inner surfaces, indicated by the red rectangles in Figure 3, are shown in Figure 4 and Figure 5 respectively where a non-uniform sub-grid is used.

Energy is transferred from the main grid to the sub-grid and the sub-grid to the main grid on the Inner and Outer Surfaces respectively.

Although the algorithm allows for a completely general choice of meshes, three restrictions are introduced in order to reduce the complexity of implementation and which do not present any significant limitations.

i. The time steps in all sub-grids must be odd integer sub-multiples of the time step in the main grid. There is no need for this sub-multiple to be the same for all sub-grids.

ii. On each surface of the boundaries, the sub-grid cell size is allowed to vary in the tangential directions but not in the normal direction

iii. The cell sizes of the main grid in the vicinity of the sub-grid boundaries must be constant.

In order to implement (i), the time steps which would be used for each grid in isolation are first calculated based on the CFL criterion with a chosen stability factor. If the calculated time steps are dt_m, dt_1, dt_2 etc. for the main grid, sub-grid 1, sub-grid 2 etc. respectively, then the time step used for sub-grid 1 is chosen to be:

$$\frac{dt_m}{\left|\dfrac{dt_m}{dt_1}\right| + 1} \tag{1}$$

and similarly for all the other sub-grids.

Constraint (ii) is not likely to present any difficulty since, for practical reasons, the sub-grid boundary will have been chosen to be several cells away from the nearest geometrical feature. This is the case for the examples given in Section III.

Similarly, in almost all practical cases, there is no need to violate constraint (iii) since any fine geometrical features in the vicinity of the boundary will have been placed in the sub-grid region, rather than the main grid region.

A. Interpolation at the Inner Surface

Figure 4 shows a portion of the mesh surrounding the $-\hat{u}$ boundary on the surface, IS, which is nominally in between the rows of E and H field nodes, shown in green. As previously [7], for each E field node on the boundary in the sub-grid, the value of **H** in the main grid at the position of the adjacent H node in the sub-grid, is approximated. This is done by interpolating from the surrounding main grid H field nodes. The E field nodes are shown as green crosses and the corresponding H field nodes are shown as green circles. From this, the value of $\mathbf{J_s}$ is calculated using $\underline{J}_s = -\underline{\hat{u}} \times \underline{H}$. The components of $\mathbf{J_s}$, tangential to the boundary are then added to the E field update equations. For example the update equation for E_v becomes:

$$E^{n+1}_{v(p+1,q,r)} = E^{n}_{v(p+1,q,r)} - \frac{\delta t}{\varepsilon \delta u}\left(H^{n+0.5}_{w(p+1,q,r)} - H^{n+0.5}_{w(p,q,r)}\right)$$
$$+ \frac{2\delta t}{\varepsilon\left(\delta v_q + \delta v_{q-1}\right)}\left(H^{n+0.5}_{u(p,q,r+1)} - H^{n+0.5}_{u(p,q,r)}\right) \tag{2}$$
$$- \frac{\delta t}{\varepsilon} J^{n+0.5}_{(p,q,r)} \cdot \underline{\hat{v}}$$

where (p,q,r) is the index of the cell containing the target H node and the current density, **J**, is given by $\underline{J} = \frac{1}{\delta u}\underline{J}_s$ since the equivalent surface current is assumed to be uniformly distributed over the volume of the cell. In the tangential directions, $\hat{v}$ and $\hat{w}$, adjacent cells may have different sizes so, when the affected node is on the cell edge, the size used is the average of the cells on each side. Since the cell size is constant in the $\hat{u}$ direction at the boundary, there is no need to use cell size averaging in this case.

The updates for the H field nodes are done in an analogous manner. For example:

$$H_{w(p,q,r)}^{n+0.5} = H_{w(p,q,r)}^{n-0.5} + \frac{\delta t}{\mu \delta v}\left(E_{u(p,q+1,r)}^{n} - E_{u(p,q,r)}^{n}\right)$$

$$-\frac{\delta t}{\mu \delta u}\left(E_{v(p+1,q,r)}^{n} - E_{v(p,q,r)}^{n}\right) \qquad (3)$$

$$-\frac{\delta t}{\mu} \underline{M}_{(p+1,q,r)}^{n} \cdot \hat{w}$$

where:

$$\underline{M} = \frac{1}{\delta u} \underline{M}_{s}$$

Since the H nodes are in the centre of the cell faces, no cell size averaging is necessary.

B. Distribution at the Outer Surface

Figure 5 shows a portion of the $-\hat{u}$ boundary on the surface, OS where the surface is nominally in between the rows of E and H field nodes which are shown in green. As previously, [7], for each boundary H field node in the sub-grid, shown as a green circle, the value of **J_s** is calculated using $\underline{J}_{s} = -\hat{u} \times \underline{H}$.

This current is distributed to the surrounding H nodes in the main grid, as indicated by the black arrows, using the same weightings as were used for the inner surface interpolation. These distributed currents are then added to the update equations for the E nodes located half a cell in the *x* direction shown by the blue arrows. For example:

$$E_{y(i+1,j,k)}^{n+1} = E_{y(i+1,j,k)}^{n} - \frac{\delta t}{\varepsilon \delta x}\left(H_{z(i+1,j,k)}^{n+0.5} - H_{z(i,j,k)}^{n+0.5}\right)$$

$$+\frac{\delta t}{\varepsilon \delta y}\left(H_{x(i,j,k+1)}^{n+0.5} - H_{x(i,j,k)}^{n+0.5}\right) \qquad (4)$$

$$-\frac{\delta t}{\varepsilon} \underline{J}_{(i,j,k)}^{n+0.5} \cdot \hat{y}$$

The current density J_y, is given by:

$$\underline{J}_{y} = \underline{J}_{sy} \frac{\delta v(\delta w + \delta w)}{2\delta x \delta y \delta z} \qquad (5)$$

where the ratio of the areas of the sub-grid and main grid cells has been included.

C. Stability issues

A further difference between the scheme used here and the one used in [7] results from the fact that the ratio of the cell sizes in the two grids can be freely chosen. When the energy is distributed from the finer grid to the coarser grid using the

field values on the E field nodes in the sub-grid at the boundary, there is a choice for the distance between the row of E nodes and the row of H nodes which are used. It has been found that the accuracy of the result is only weakly affected by this choice but that the stability performance is best when the spacing is chosen to be as close as possible to half the size of the main grid cell. In the case shown in the Figure 5, the ratio of the main grid cell size to the size of the sub-grid cells in the normal direction is 3, so the E and H field rows are separated by 1.5 sub-grid cells instead of 0.5 sub-grid cells as previously.

In [7], following [5], a spatial filter was introduced in order to suppress the dominant mode of instability. The method, which is described in detail in [7], is applied both to the field interpolation at the Inner Surface and to the field distribution at the Outer Surface. In the example shown in Figure 4, instead of interpolating directly from the H field nodes, spatially averaged values are used. For example, instead of using the value of H at the node $H_{i,j,k}$, the averaged value given by (6) would be used. Similarly for the other H field values used in the interpolation.

$$\overline{H}_{i,j,k} = \frac{H_{i-1,j,k}}{8} + \frac{H_{i,j-1,k}}{8} + \frac{H_{i,j,k-1}}{8}$$

$$+\frac{H_{i,j,k}}{4} \qquad (6)$$

$$+\frac{H_{i+1,j,k}}{8} + \frac{H_{i,j+1,k}}{8} + \frac{H_{i,j,k+1}}{8}$$

Similarly for the example shown in Figure 5, instead of distributing to the node $H_{i,j,k}$, a weighted distribution is made to the surrounding modes using the same weighting as used in (6).

This filter is designed to suppress the build up of spurious field patterns which have a high spatial frequency. Since this filtering and redistribution is applied only to the main grid, which remains uniform, the introduction of a non-uniform sub-grid does not require any change compared to that used in [7]. As will be shown in Section V, it has been found that this spatial filtering is equally beneficial when non-uniform sub-grids are in use as it is when the sub-grid is uniform.
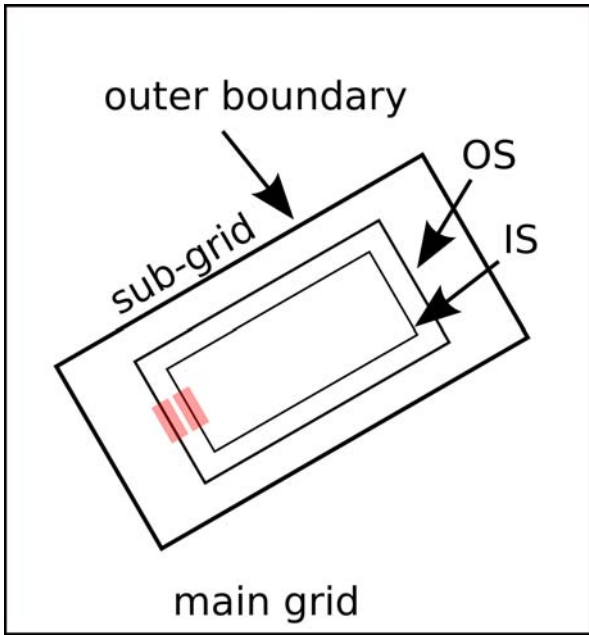
Figure 3 - Section through the rotated sub-grid showing boundary surfaces
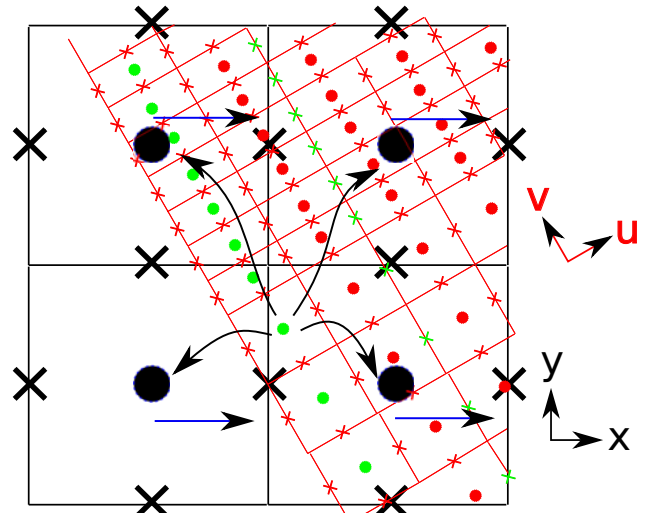

Figure 4 - Detail of H field interpolation

Figure 5 - Detail of H field distribution

III. RESULTS

A. Plane wave propagation through the sub-grid

As a first test in order to investigate the effect of allowing non-uniformity in the grid, a simple problem was set up to examine the propagation of a plane wave through the sub-grid region. The test structure is the same as was used in [7], and is shown in Figure 7a, but now it is used with a non-uniform grid. The size of the main grid is (1500,375,375)mm. A sub-grid is placed in the main grid with its centre at (450,186,186)mm and with a size of (300,75,75)mm. The structure is excited with a plane wave pulse, propagating in the *x* direction and with a width of 439ps, corresponding to a peak frequency of 2.3GHz. The main grid has a uniform cell size of 3mm and the sub-grid has a non-uniform cell size which varies from 1mm down to 0.25mm in the *v* and *w* directions as shown in Figure 6. The time variation of the E field was recorded in the main grid at positions of 150mm, 185mm, 700mm and 750mm and, in the sub-grid, at positions of 60mm, 150mm and 240mm from the left hand boundary of the sub-grid. The time step used in the main grid was 5.2ps corresponding to a stability factor of 0.9. In the sub-grid the time step was 0.74ps which is 1/7 of the main grid time step and corresponds to a stability factor of 0.67. Figure 7a shows the places at which the field amplitudes are observed. The red circles show the positions of the observation points in the main grid and the green circles show the positions of the observation points in the sub-grid.
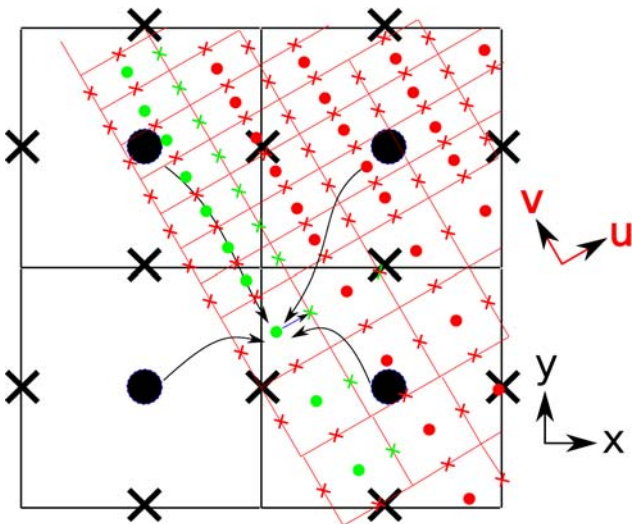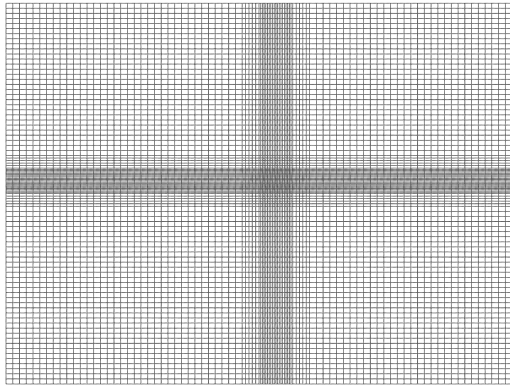
Figure 6 - Sub-grid mesh for plane wave propagation

In Figure 7b results are shown for the case where the sub-grid is rotated by 30° with respect to the main grid. It can be seen that the pulse propagates with little distortion.

The level of reflection caused by the sub-grid was calculated by observing the amplitude of the incident and reflected pulse as recorded at the leftmost main grid observation point. Figure 8 shows results for frequencies up to 5GHz, which corresponds to a main grid cell size of one twentieth of a wavelength, and for various angles of rotation. For comparison, the corresponding results for a uniform sub-grid having a cell size of 1mm is shown in Figure 9. It can be seen that, in both cases, the reflection is less than -50dB over much of the frequency range and angles of rotation and it is similar for the uniform and the non-uniform cases.
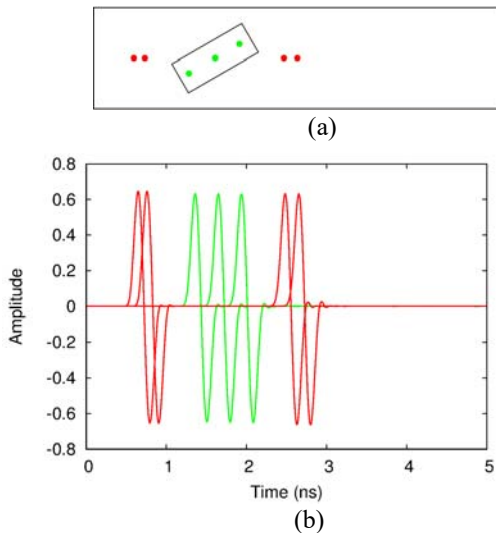

(a)

(b)

Figure 7 - Propagation through a non uniform grid rotated by 30 degrees
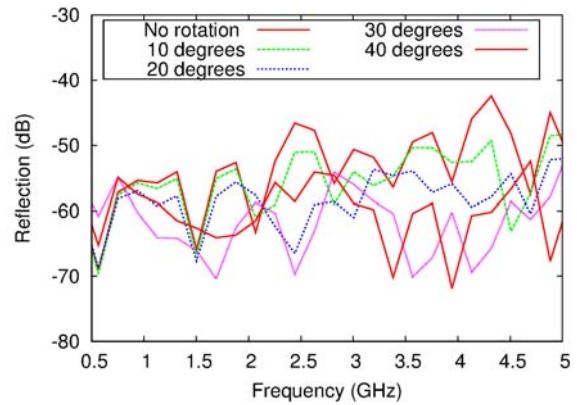

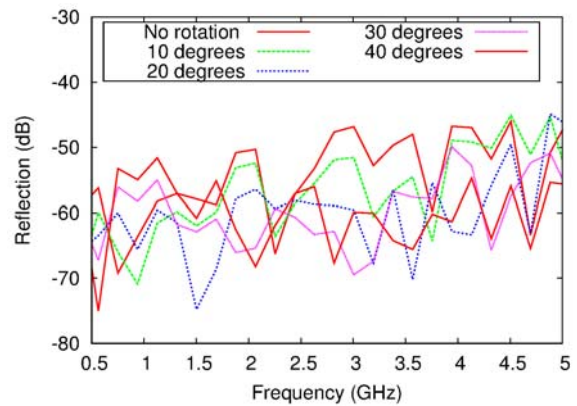**Figure 8 - Reflection from non-uniform sub-grids at various angles of rotation**

Figure 9 - Reflection from uniform sub-grid with various angles of rotation

B. Characterisation of the MARIA array.

An example of the application of this method to a more realistic situation is the characterization of the MARIA antenna array. In order to do this efficiently, the details of each element are represented by the graded sub-grid shown in Figure 10 and Figure 11 which also show the material boundaries. The mesh used is similar to that used in [9] and the cell sizes are between 0.2mm and 0.47mm. These have been chosen so that the small features are covered by smaller cells and the positions of the cell boundaries are chosen for best accuracy.

The main grid is uniform with a cell size of 1mm. The time step for the main grid was 1.8295ps, corresponding to a stability factor of 0.95. In order to allow for the an integer ratio between the time step in the main grid and the sub-grid, the time step in the sub-grid was set to 0.26ps which is 1/7 of the main grid time step.

A direct FDTD simulation of the complete array would take an impractically long time so, in order to compare the results with those from a direct FDTD analysis, a simplified model was used for which comparison results could be obtained. This consisted of retaining just three of the original 31 elements labeled as 1, 2 and 5 in Figure 1. For the comparison, the hemisphere was filled with a dielectric having a relative

permittivity of 9. This simplified structure was modeled using a state-of-the-art commercial FDTD program and also using the method described in this paper. The commercial program required 8 days to obtain results for each transmit antenna element whereas the present method required only 36 hours for a simulation time of 15ns, a five-fold saving. Moreover, the commercial program was run on a dual quad core Intel Xeon E5405 processor running at 2GHz whereas the present method was run on one core of the less powerful Intel core 3 processor.

In each of the numerical experiments which follow, the results from simulations using direct FDTD simulations are compared with those obtained using the non-uniform sub-grid approach.
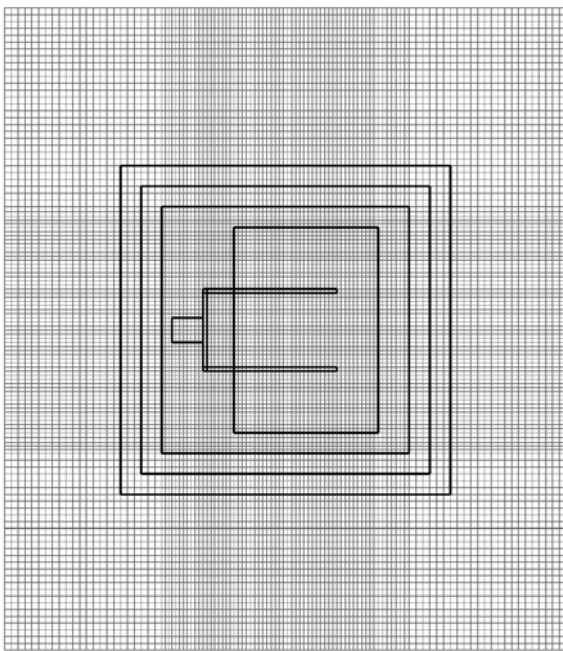

Figure 10 - Non-uniform sub-grid for the y-plane of each CBS element

In Figure 12 and Figure 13 the transient responses are shown. It can be seen that, while there are some discrepancies, there is generally good agreement. The corresponding frequency domain results are shown in Figure 14 and Figure 15 and, again, reasonable agreement is obtained with discrepancies of approximately 5dB over much of the frequency range. The level of agreement is similar to that found using the method of [9].

In order to check for instability, the simulations were run for 16384 main grid iterations, a simulated time of 30ns, and no sign of instability was observed.
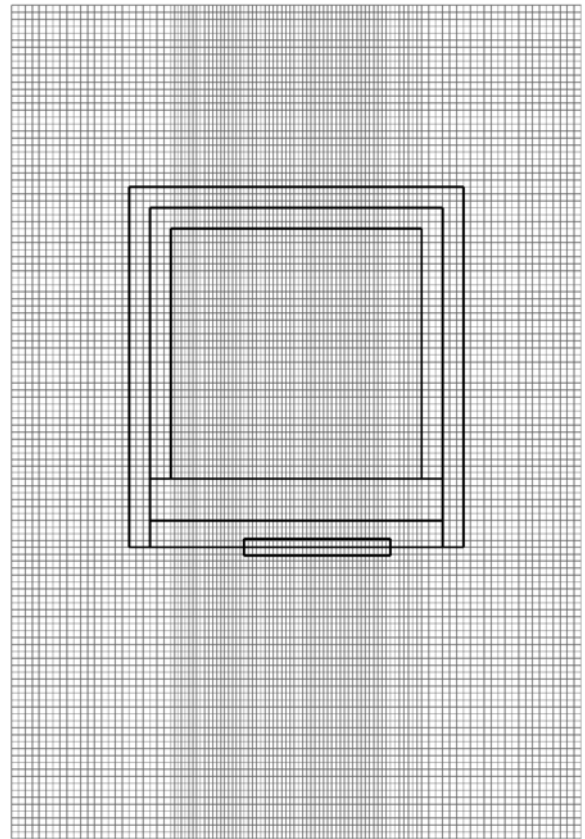

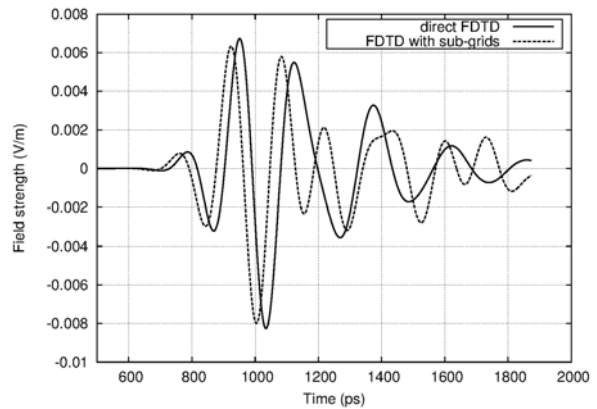**Figure 11 - Non-uniform sub-grid for the z plane of each CBS element**

Figure 12 - Transient response at element 2 caused by excitation at element 1 using direct FDTD and FDTD with sub-grids
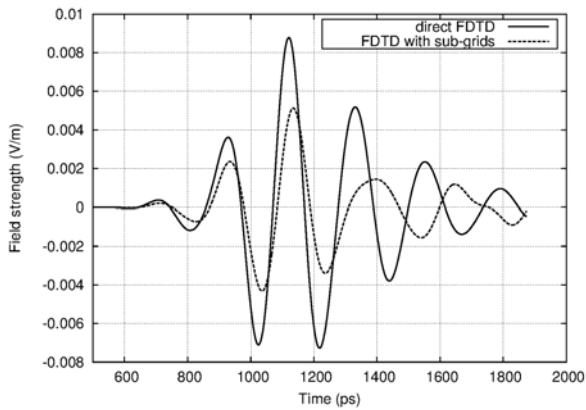
Figure 13 - Transient response at element 5 caused by excitation at element 1 using direct FDTD and FDTD with sub-grids
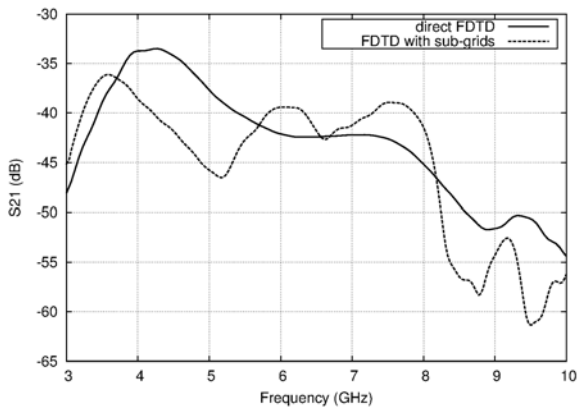

Figure 14 - Frequency response at element 2 caused by excitation at element 1
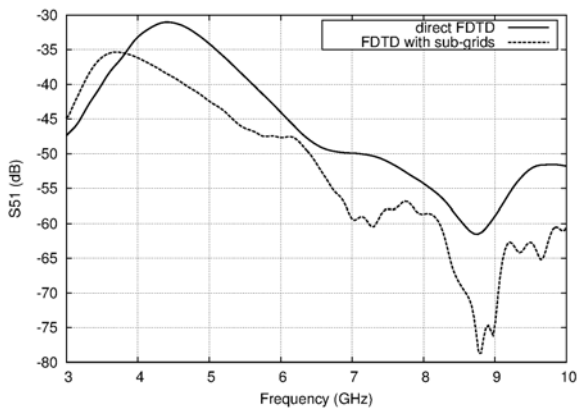

Figure 15 - Frequency response at element 5 caused by excitation at element 1

IV. CONSISTENCY CHECKS

In order to check that the algorithm gives consistent results with different mesh sizes and different time steps, the structure described in Section III.B was modeled using three different meshes as specified in Table 1. These required that the ratios

between the main grid time step and the sub-grid time step be 7, 9 and 3 respectively.

The results for the calculated transient responses at elements 2 and 5, in response to excitation at element 1, are given in Figure 16 and Figure 17 respectively. In each case the calculated responses using the three different mesh configurations are shown. It can be seen that very good agreement is obtained.

Table 1 - Meshes used for characterisation of the MARIA array

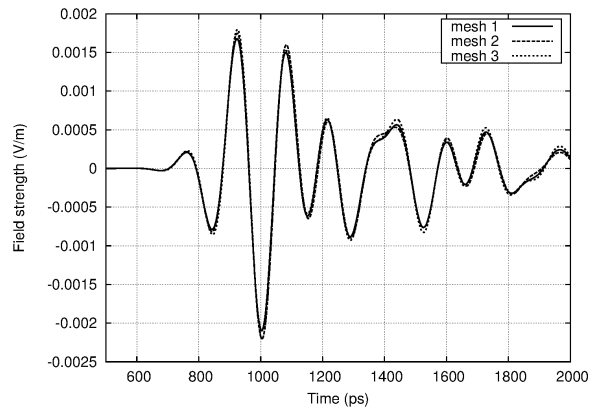| Main grid cell size	Main grid time step	Sub-grid largest cell size	Sub-grid smallest cell size	Sub-grid time step
1mm	1.83ps	0.47mm	0.2mm	0.26ps
1mm	1.83ps	0.34mm	0.17mm	0.203ps
0.5mm	0.915ps	0.47mm	0.2mm	0.305ps

Figure 16 - Transient response at element 2 caused by excitation at element 1 using different meshes.
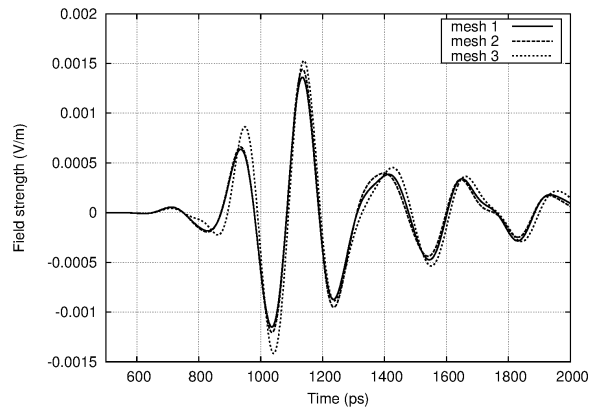

Figure 17 - Transient response at element 5 caused by excitation at element 1 using different meshes.

V. STABILITY CHECKS

In order to demonstrate the stability properties of the method, and to show the effect of non-uniformity on the stability, a test case, similar to the scenario shown in Figure 7a was used. The main grid had a size of (200,200,200)mm and the subgrid was

centrally placed and had a size of (50,50,50)mm. This was run until instability became apparent. The results are shown in Figure 18 - Figure 21 for the cases of (i) a uniform sub-grid with a cell size of 1mm and (ii) a non-uniform sub-grid with cell sizes varying between 0.25mm and 1mm, similar to that shown in Figure 6. In each case, results are shown for unrotated sub-grid and a sub-grid rotated by 30$^\text{O}$. The different lines in these plots give the field values at different probe points as indicated in the legend. The positions of the subgrid probes are relative to the lower left hand corner of the subgrid. Generally it can be seen that, although the instability becomes visible at slightly different times in different places, once it starts, it rapidly spreads throughout the entire mesh.

It is shown that, for all four cases the onset of instability is at approximately 300ns simulation time, corresponding to approximately 60,000 main grid iterations. This indicates that using a non-uniform sub-grid imposes no penalty in terms of stability. For most practical cases, this is an ample number of iterations to obtain the desired results.

It is noted that, after having suppressed the dominant instability mode using spatial filtering, the mode of the remaining instability is different from that previously observed and takes the form of a steady exponential growth instead of an oscillation. The origin of this instability is not currently known and is being investigated. Nevertheless, the onset of this mode of instability is not until well beyond the simulation time observed in [7] for a similar geometry and mesh size.
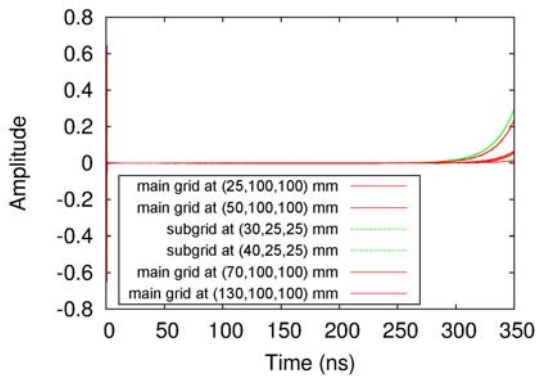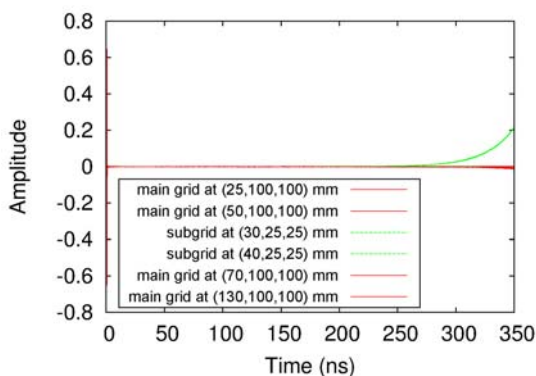

Figure 18 - Stability of unrotated uniform mesh
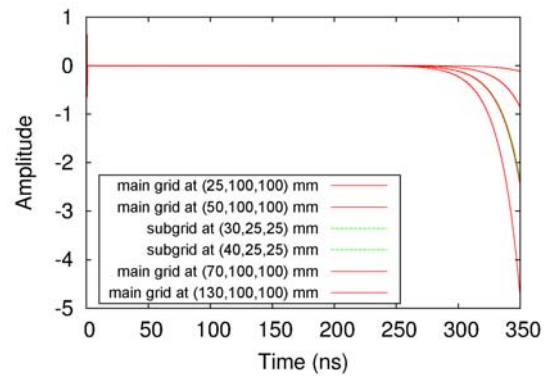

Figure 19 - Stability of uniform mesh rotated by 30$^\text{O}$

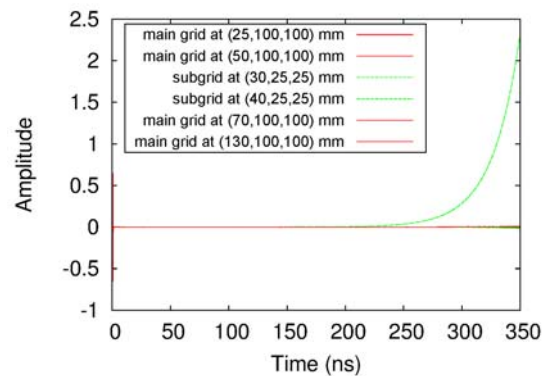**Figure 20 - Stability of unrotated non-uniform mesh**

Figure 21 - Stability of non-uniform mesh rotated by 30$^\text{O}$

VI. CONCLUSIONS

In this paper, a novel method for allowing rotated, non-uniform, sub-grids to be used in the FDTD method has been presented. It has been shown by means of several examples that using a non-uniform sub-grid does not cause any significant loss in accuracy or reduction of stability in most practical cases. The method has been applied to the characterisation of a large conformal array of Cavity Backed Slot antennas which themselves are complicated structures. The results obtained give good agreement with direct FDTD analyses but with a saving in computer resources of over five-fold.

REFERENCES

[1] Kane Yee, "Numerical Solution of initial boundary value problems involving Maxwell's equations in isotropic media", IEEE Trans. on Antennas and Propagation, Vol 14, No. 5, May 1966, pp 302-307

[2] Allen Taflove and Susan C. Hagness, "Computational Electrodynamics: The Finite Difference Time Domain Method", 3$^\text{rd}$ edition, Artech House Publishers, 2005, ISBN 1-58053-832-0

[3] M. Okeniewski, E. Okoniewska and M. Stuchly, "Three dimensional subgridding algorithm for FDTD", IEEE Transactions on Antennas and Propagation, Vol 45, No. 3, March 1997, pp 422-429

[4] P. Thoma and T. Weiland, "A consistent subgridding scheme for the finite difference time domain method," Int. J. Num. Model.: Electron. Network, Devices Fields, vol. 9, pp. 359–374, 1996.

[5] Jean-Pierre Bérenger, "The Huygens subgridding for the numerical solution of the Maxwell equations", Journal of Computational Physics, 230 (2011) pp. 5635-5659.

[6] Oliver Podebrad, Markus Clemens and Thomas Weiland, "New Flexible Subgridding Scheme for the Finite Integration Technique", IEEE Trans. Magnetics, Vol. 39, No. 3, May 2003, pp. 1662-1665.

[7] Chris J. Railton, "Rotated Sub-grids in the FDTD Method" IEEE Trans. On Antennas and Propagation, Vol. 64, No. 7, July 2016, pp 3047-3054.

[8] M. Klemm, J. Leendertz, D. Gibbins, I.J. Craddock, A. Preece, R. Benjamin, "Towards Contrast Enhanced Breast Imaging using Ultra-Wideband Microwave Radar System" , Radio and Wireless Symposium (RWS), 2010, pp. 516-519

[9] C Christodoulou, C. J. Railton, M. Klemm, D. Gibbins, I. J. Craddock, "Analysis of a UWB hemispherical antenna array in FDTD with a Time Domain Huygens method", IEEE Trans. On Antennas and Propagation, Vol. 60, No. 11, Nov. 2012, pp 5251-5258.

Chris Railton received the BSc degree in Physics with Electronics from the University of London in 1974 and the PhD degree in Electronic Engineering from the University of Bath in 1988. During the period 1974-1984 he worked in the scientific civil service on a number or research and development projects in the areas of communications, signal processing and EMC. Between 1984 and 1987 he worked at the University of Bath on the mathematical modelling of boxed microstrip circuits. From 1987 until 2015 he worked in the Centre for Communications Research at the University of Bristol where he was engaged in research in the development of new algorithms for electromagnetic analysis, especially those related to the Finite Difference Time Domain method. Dr. Railton retired in 2015 and is now an Emeritus Professor at the University of Bristol.